Velocity Distribution of Ions Incident on a Radio-Frequency Biased Wafer

G. Wakayama and K. Nanbu

Institute of Fluid Science, Tohoku University, Katahira 2-1-1, Aoba-ku, Sendai, Japan 980-8577

Abstract. The ion velocity distribution (IVD) is important in plasma etching of microfeatures. IVD at a rf biased wafer is studied, first analytically using probability theory and then numerically by using a particle simulation method. The analytic expression shows that IVD is governed by the parameter $qV_{\rm rf}/m_{\rm i}\omega l$, where q is the charge of ion, $V_{\rm rf}$ is the rf bias amplitude, ω is the rf bias angular frequency, l is the penetration depth of bias potential, and $m_{\rm i}$ is the mass of ion. The analytical expression is applicable to the case when the ion collisions in the penetration depth are negligibly few and the rf period of biasing is much shorter than the time that ions take in traversing the depth l. The IVDs for general conditions are also examined using the self-consistent particle-in-cell/Monte Carlo simulation.

I INTRODUCTION

Weakly ionized plasmas used in materials processing generally consist of positive and negative ions, electrons, and neutral species. In the case when electrons are more abundant than negative ions, a negative potential is formed near the surface of the floating wafer immersed in the plasma. In processing plasmas the electron temperature is few electron volts, while the ion temperature is roughly equal to the background gas temperature. To keep the balance between the negative and positive currents on the floating surface, low energy electrons should be reflected in the sheath region back to the plasma bulk. This is the physical reason why the potential of the floating wafer is lower than the plasma potential.

Negative sheath potential (measured from the plasma bulk) accelerates the positive ions to the wafer. If no collision is assumed in the sheath region, the positive ions impinge almost perpendicularly onto the wafer. However, electrons are decelerated and lose the velocity component normal to the wafer.

When ions and electrons come into a microscopic trench, electrons are easily sticked near the top of the side of the trench wall while ions can reach the bottom of the trench. This kind of charge separation inside microfeatures causes a charge build-up. The strongly localized electric field due to the charge build-up distorts the trajectories of incident ions, which results in an anomalous etch profile called "notching". The localized charge build-up also causes the electrical breakdown induced by fatal tunneling currents through gate-oxides.

In order to suppress the so-called charging damages, new ideas on plasma sources are proposed, e.g., time-modulation of the source power [1] and use of ultra-high frequency (500 MHz) power [2]. These approaches are intended to lower the electron temperature and hence generate more negative ions. To understand the role of negative ions, let us consider the plasma including only positive and negative ions; when the wafer is biased at low frequency ($\lesssim 3$ MHz), the positive and negative ions impinge on the bottom of the trench alternately. Thus no charge build-up occurs.

The ion energy distribution (IED) and ion angle distribution (IAD) of ions that impinge on a biased wafer are important to clarify the mechanism of etching and charging damage of microfeatures. In low gas pressure and high plasma density, the rf wafer biasing is employed for controlling incident ion energy independently of the source power. Sobolewski *et al.* [3] measured the IEDs for various bias amplitudes and frequencies in a planar inductively-coupled plasma (ICP) reactor. Hoekstra and Kushner [4] calculated the IEDs in an ICP. They discussed the effects of the bias amplitude, gas pressure, and source power on the IED. Notching can be explained from charging of the surfaces of microfeatures. Kinoshita *et al.* [5] presented the relationship between the charging potential and the IED. Hasegawa *et al.* [6] reported that an appropriate rf biasing suppresses the

CP585, *Rarefied Gas Dynamics: 22nd International Symposium*, edited by T. J. Bartel and M. A. Gallis

REPORT DOCUMENTATION PAGE

Form Approved OMB No. 0704-0188

1. REPORT DATE (DD-MM-YYYY)	2. REPORT TYPE	3. DATES COVERED (FROM - TO)
09-07-2000	Conference Proceedings	09-07-2000 to 14-07-2000

4. TITLE AND SUBTITLE
Velocity Distribution of Ions Incident on a Radio-Frequency Biased Wafer
Unclassified

5a. CONTRACT NUMBER
5b. GRANT NUMBER
5c. PROGRAM ELEMENT NUMBER

6. AUTHOR(S)
Wakayama, G. ;
Nanbu, K. ;

5d. PROJECT NUMBER
5e. TASK NUMBER
5f. WORK UNIT NUMBER

7. PERFORMING ORGANIZATION NAME AND ADDRESS
Institute of Fluid Science
Tohoku University
Katahira 2-1-1, Aoba-ku
Sendai, Japan980-8577

8. PERFORMING ORGANIZATION REPORT NUMBER

9. SPONSORING/MONITORING AGENCY NAME AND ADDRESS
AOARD
Unit 45002
APO AP, xx96337-5002

10. SPONSOR/MONITOR'S ACRONYM(S)
11. SPONSOR/MONITOR'S REPORT NUMBER(S)

12. DISTRIBUTION/AVAILABILITY STATEMENT
APUBLIC RELEASE
,

13. SUPPLEMENTARY NOTES
See Also ADM001341, Rarefied Gas Dynamics (RGD) 22nd International Symposium held in Sydney, Australia, 9-14 July 2000.

14. ABSTRACT
The ion velocity distribution (IVD) is important in plasma etching of microfeatures. IVD at a rf biased wafer is studied, first analytically using probability theory and then numerically by using a particle simulation method. The analytic expression shows that IVD is governed by the parameter qVrf/miU)l, where q is the charge of ion, VTf is the rf bias amplitude, uj is the rf bias angular frequency, / is the penetration depth of bias potential, and mi is the mass of ion. The analytical expression is applicable to the case when the ion collisions in the penetration depth are negligibly few and the rf period of biasing is much shorter than the time that ions take in traversing the depth I. The IVDs for general conditions are also examined using the self-consistent particle-in-cell/Monte Carlo simulation.

15. SUBJECT TERMS

16. SECURITY CLASSIFICATION OF:			17. LIMITATION OF ABSTRACT	18. NUMBER OF PAGES	19. NAME OF RESPONSIBLE PERSON
a. REPORT	b. ABSTRACT	c. THIS PAGE	Public Release	8	Fenster, Lynn lfenster@dtic.mil
Unclassified	Unclassified	Unclassified			19b. TELEPHONE NUMBER International Area Code Area Code Telephone Number 703767-9007 DSN 427-9007

charging damage.

Nasser *et al.* [7] found that the penetration depth of the potential oscillation due to rf biasing is much larger than the Debye length. Thus the IED is greatly affected by the potential oscillation. In this report we consider two approaches for obtaining the IVD at a rf biased wafer. First, using the probability theory, we obtain the IVD analytically under certain simplified situations. The obtained expression shows that the IVD is governed by a similarity plasma parameter. Second, using self-consistent particle-in-cell/Monte Carlo simulation, we determine the oscillatory sheath potential due to rf biasing and hence obtain the IVDs.

II ANALYTICAL ION VELOCITY DISTRIBUTION

First we obtain the IVD analytically using the probability theory [8]. Ahn [9] measured the instantaneous plasma potential in the ICP. The potential that is time-modulated by high frequency biasing is well approximated by the exponentially attenuating sine curve. In this case, the velocity of ion normal to the wafer, $v_{\rm w}$, can be expressed as $v_{\rm w} = \overline{v}_{\rm w} + \widetilde{v}_{\rm w}$, where $\overline{v}_{\rm w}$ is the contribution from a time-averaged potential and $\widetilde{v}_{\rm w}$ is that from an oscillatory part of the potential [10]. For high frequency biasing, we found that the time when the ion impinges on the wafer is uniformly distributed. Assuming no collision, we can then obtain the probability density function $G(\widetilde{v}_{\rm w})$ for the time-modulated velocity $\widetilde{v}_{\rm w}$

$$G(\widetilde{v}_{\rm w}) = \frac{1}{\pi\sqrt{A^2 - \widetilde{v}_{\rm w}^2}}, \tag{1}$$

where A is given by

$$A \simeq \frac{qV_{\rm rf}}{m_{\rm i}\omega l}. \tag{2}$$

Here $m_{\rm i}$ is the mass of ion, q is the charge of ion, $V_{\rm rf}$ is the amplitude of the rf bias, l is the penetration depth of the biasing potential, and ω is the bias angular frequency. The probability density function $H(\overline{v}_{\rm w})$ for $\overline{v}_{\rm w}$ can be obtained by assuming that ions in the plasma bulk are in equilibrium. Now the probability density function $F_{\parallel}(v_{\rm w})$ for the sum $v_{\rm w} = \overline{v}_{\rm w} + \widetilde{v}_{\rm w}$ is given by the convolution of $G(\widetilde{v}_{\rm w})$ and $H(\overline{v}_{\rm w})$

$$F_{\parallel}(v_{\rm w}) = \int G(v_{\rm w} - v)H(v)\mathrm{d}v. \tag{3}$$

To check the validity of the analytical IVD, we separately determined the IVD from numerical solutions of the equation of motion and compared the two results. The best fitting of Ahn's [9] experimental data of potential becomes $\phi(x,t) = 4.5 + 0.019x + 2.4 \times 10^{-4}x^2 - 16\exp(-x/2.1) + 55\exp(-x/2.8)\sin(\omega t)$, where x in units of mm is the normal distance measured from the wafer at $x = 0$. The rf bias frequency is 15 MHz. We calculated the motion of Cl_2^+ ions. Figure 1 shows the comparison of the analytical and numerical IVDs. The analytical expression shows a good agreement with the numerical solution. In Fig. 1, the distance between the two peaks is $2A(= 2qV_{\rm rf}/m_{\rm i}\omega l)$.

III SELF-CONSISTENT PIC/MC SIMULATION

It is clear that the IVD is a functional of the sheath potential $\phi(x,t)$, which depends on the wafer biasing and collisions. In the case when there is no experimental data on $\phi(x,t)$, it is necessary to calculate $\phi(x,t)$ and IVD simultaneously. In order to examine the effects of bias frequency and ion collisions on IVD, the self-consistent particle-in-cell/Monte Carlo simulation is employed.

The background gas is argon which is assumed to be uniform and in equilibrium at temperature of 300 K. Although e^-, Ar^+, and Ar are taken into consideration in the present calculation, we have only to examine the motion of e^- and Ar^+. The velocity of Ar is necessary only when determining the postcollisional velocity of e^- or Ar^+.

Since the number density of charged species is less than $10^{17}\,\mathrm{m}^{-3}$ in the present problem, Coulomb collisions (e^-–e^-, Ar^+–Ar^+ and e^-–Ar^+) can be neglected and therefore we consider e^-–Ar and Ar^+–Ar collisions. For e^-–Ar collisions, elastic collision, ionizing collision, and also 25 exciting collisions are taken into consideration

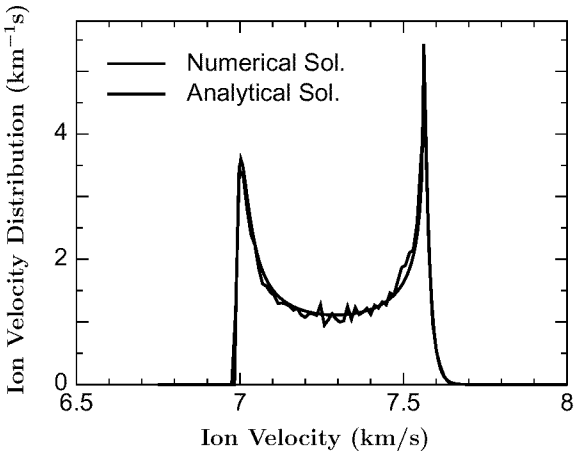

FIGURE 1. Ion velocity distributions (no collision).

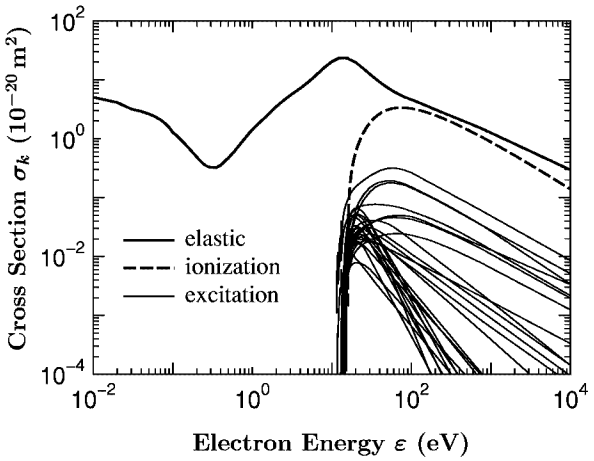

FIGURE 2. Cross sections for e^-–Ar collision.

based on a set of the cross section data of Kosaki and Hayashi [11]. As for ionization, Peterson and Allen's [12] integral cross section is multiplied by 0.9 to match it with Kosaki and Hayashi's data. The total number of collisional events is 27. Each event is expressed by k ($k = 1, 2, \cdots, 27$); k = 1–25 for excitation, $k = 26$ for ionization, and $k = 27$ for elastic collision. The cross section σ_k for e^-–Ar collision is shown in Fig. 2. The probability of occurrence of the kth event in time Δt is

$$P_e(k) = N_B \sigma_k(\varepsilon) \left(\frac{2\varepsilon}{m_e}\right)^{1/2} \Delta t, \tag{4}$$

where N_B is the number density of background argon gas, ε is the electron energy, and m_e is the electron mass.

Elastic collision and resonant charge exchange are considered for the Ar^+–Ar collision. The simple and computationally efficient model proposed in our previous work [13], the use of which was shown to reproduce the measured data of ion drift velocity and transverse diffusion coefficient, is employed. The model is a combination of isotropic scattering and charge switching, both occurring with the same probability. The probability P_i that an ion Ar^+ collides with atom Ar in time Δt is given by

$$P_i = N_B \bar{g} \pi d_{AB}^2 \Delta t, \tag{5}$$

where $\bar{g}$ is the relative velocity between Ar^+ and Ar averaged over the Maxwellian distribution for Ar with temperature $T_B (= 300\,\mathrm{K})$ and πd_{AB}^2 is the collision cross section twice as large as πd_{BB}^2, d_{BB} being the viscosity diameter of Ar.

One time step of the simulation consists of solving the equation of motion for e^- and Ar^+, obtaining the charge density, solving the Poisson equation, and calculating collisions. The time-evolution is calculated until a periodic steady state is obtained.

The one-dimensional computational domain from the biased wafer ($x = 0$) to the plasma bulk ($x = L$) is shown in Fig. 3. The unknowns in the present problem are the dc bias V_{dc} at the wafer and the flow velocity of ions at $x = L$. The electron flow velocity at $x = L$ is equal to the ion flow velocity because of no net current in the plasma bulk. The bias V_{dc} is determined from the floating condition; the net current during one period of rf biasing is zero in periodic steady state. Ar^+ and e^- come from $x > L$ and cross the presheath edge at $x = L$. The flow velocity is determined in such a way that the plasma density is continuous at $x = L$.

The length L of the computational domain is 100 mm, as is shown in Fig. 3. Let the x–axis be in the direction normal to the wafer with the origin at the wafer. We used equally spaced grids of $\Delta x = 0.1$ mm. That is, the domain was divided into 1000 cells. Note that the Debye length is 0.11 mm for electron density of $10^{16}\,\mathrm{m}^{-3}$ and electron temperature of 2 eV. The electron time step Δt_e was determined so as to satisfy the condition that the total collision probability for electron is less than 0.03. This condition also meets the requirement for Nanbu's method [14] that the maximal probability of collisional events must be less than 1/27, where 27 is the total number of collisional events. From the requirement we chose $\Delta t_e = 9.26 \times 10^{-11}$ s at the background gas pressure $p_B = 5$ mTorr, $\Delta t_e = 5.29 \times 10^{-11}$ s at $p_B = 10$ mTorr, and $\Delta t_e = 2.65 \times 10^{-11}$ s at $p_B = 20$ mTorr. The ion time step Δt_i was chosen to be $\Delta t_i = 30 \Delta t_e$, for which the Ar^+–Ar collision probability is less than

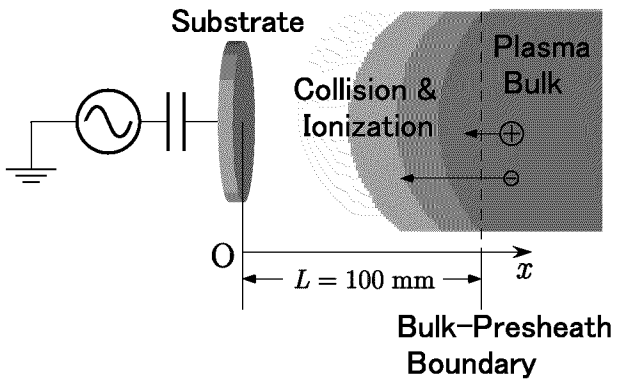

FIGURE 3. One-dimensional computational domain.

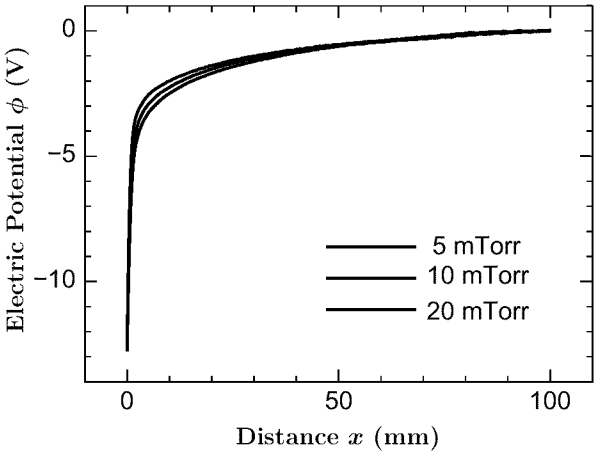

FIGURE 4. Electric potential ϕ. Wafer is at $x = 0$.

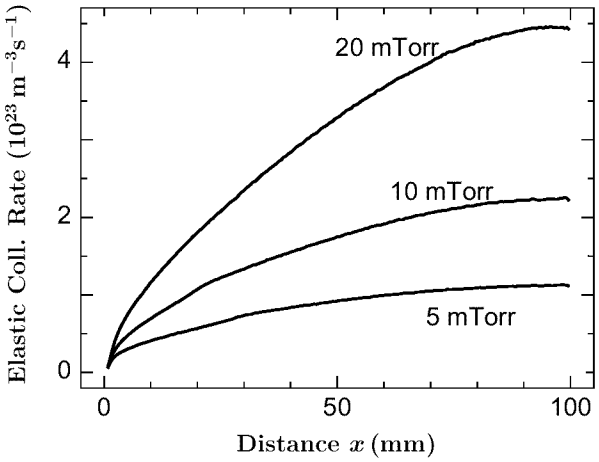

FIGURE 5. e^-–Ar elastic collision rate.

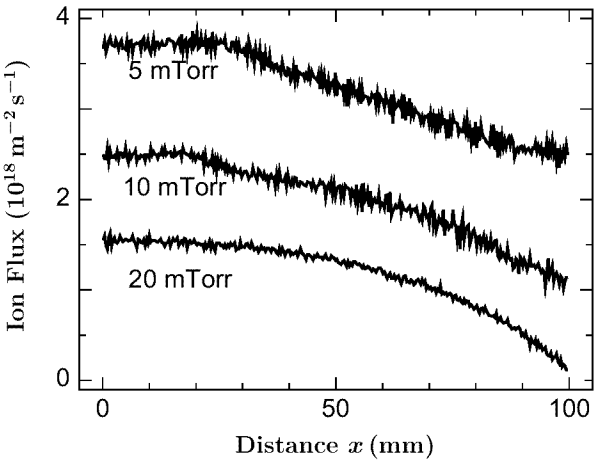

FIGURE 6. Ion flux.

0.05. Since the plasma bulk is charge-neutral, a common value of $10^{16}\,\mathrm{m}^{-3}$ was chosen as the ion and electron densities in the plasma bulk. In processing plasmas the electron temperature T_e is much higher than the ion temperature T_i due to the power deposition to electrons. Therefore we set $T_\mathrm{i} = 500\,\mathrm{K}$ and $k_\mathrm{B}T_\mathrm{e} = 2\,\mathrm{eV}$ in the plasma bulk ($x > L$), where k_B is the Boltzmann constant.

IV RESULTS AND DISCUSSION

The validity of the method described above was first examined by calculating the structure of the potential in the case of no rf biasing, the wafer being floating. Figure 4 shows the electric potential ϕ. The region $x < L(= 100\,\mathrm{mm})$ consists of the sheath plus presheath. In the presheath the charge neutrality is kept. Note that the potential in the plasma bulk is set zero. Assuming no collision for ions in the sheath and presheath results in the floating potential ϕ_f on the wafer as [15]

$$\phi_\mathrm{f} = -\frac{T_\mathrm{e}}{2} - T_\mathrm{e} \ln\left(\frac{m_\mathrm{i}}{2\pi m_\mathrm{e}}\right)^{1/2}. \tag{6}$$

As is shown later, the electron temperature in $x < L$ is almost constant and close to the value in the plasma bulk (2 eV). The floating potential ϕ_f obtained from eq. (6) is $-10.4\,\mathrm{V}$. The floating potential in Fig. 4 is $-12.29\,\mathrm{V}$ at the background gas pressure $p_\mathrm{B} = 5\,\mathrm{mTorr}$, $-12.58\,\mathrm{V}$ at $p_\mathrm{B} = 10\,\mathrm{mTorr}$, and $-12.77\,\mathrm{V}$ at $p_\mathrm{B} = 20\,\mathrm{mTorr}$. The corresponding flow velocity at $x = L$ is 327 m/s at 5 mTorr, 112 m/s at 10 mTorr, and -124 m/s at 20 mTorr. The negative flow velocity at 20 mTorr is caused by a considerable increase of the number of electrons and

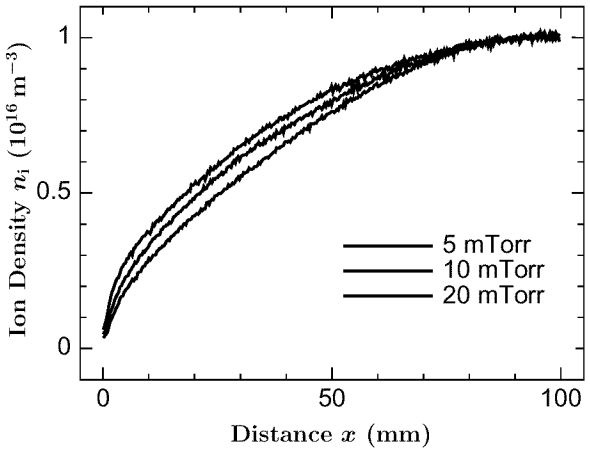

FIGURE 7. Ion density.

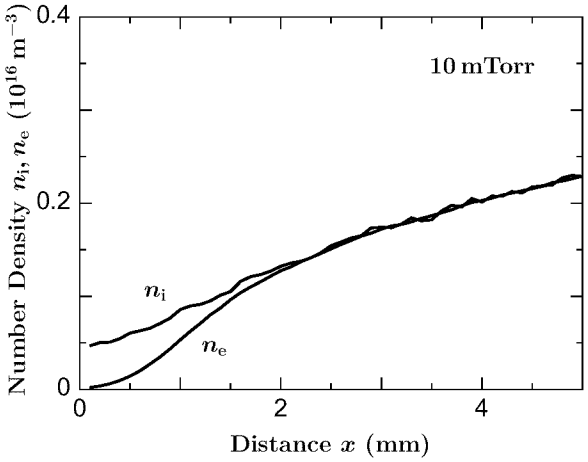

FIGURE 8. Number densities of ion and electron (10 mTorr).

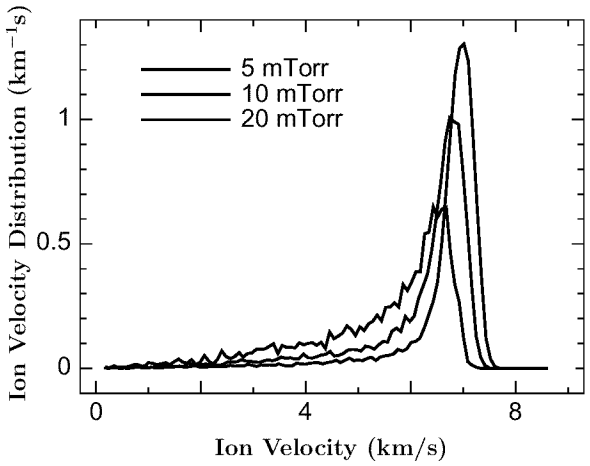

FIGURE 9. Ion velocity distribution.

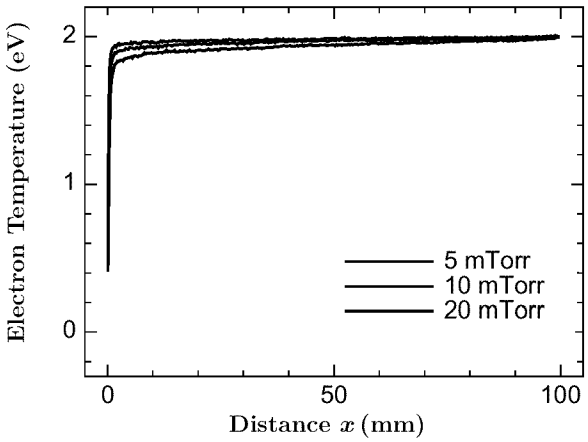

FIGURE 10. Electron temperature.

ions in $x < L$ due to ionization. The difference of ϕ_f between our data and eq. (6) is ascribable to e^-–Ar and Ar^+–Ar collisions in $x < L$. Figure 5 shows the rate for e^-–Ar elastic collision. The rate is proportional to the gas pressure and the electron density n_e approximately. The rate decreases with x because n_e decreases with x, as is shown later. The ionization rate is about 4 orders smaller than the elastic collision rate. As we have seen, however, ionization has a large effect near the outer boundary of the computational domain. Also ion (electron) flux is not constant due to ionization. This is shown in Fig. 6. Electrons are decelerated by e^-–Ar collisions and ions are by Ar^+–Ar collisions. The fact that ϕ_f determined from the simulation is lower than the collisionless ϕ_f given by eq. (6) means that the collisional deceleration is stronger for Ar^+–Ar collision than e^-–Ar collision, thus requiring a lower ϕ_f to accelerate ions and satisfy the floating condition on the wafer. The larger collisional deceleration for Ar^+–Ar is due to charge-exchange collisions.

Where is the boundary between the sheath and presheath? Figure 7 shows the ion density n_i. The electron density n_e almost agrees with n_i except the region close to the wafer. This region is enlarged in Fig. 8 at $p_B = 10$ mTorr. We see that the charge neutrality breaks near $x = 2$ mm. This location is the boundary between the sheath and presheath. Figure 9 shows the ion velocity distribution function. The distribution is more localized as pressure and hence, the ion collision frequency decreases. The upper limit in the right side of the peak represents the ion velocity in the case of no collision. We show the electron temperature in Fig. 10. The change in the temperature is very small in the presheath. As pressure increases, the electron temperature in the presheath slightly decreases due to the increase of the rate of inelastic e^-–Ar collisions. The rapid decrease near the wafer is due to the sharp decrease of the potential in the sheath. The ion temperature is also

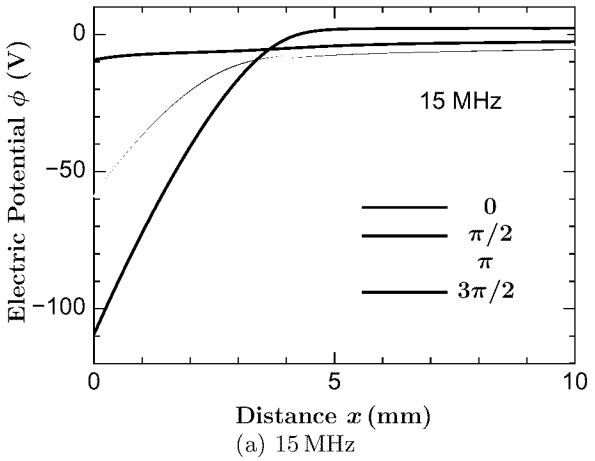

(a) 15 MHz

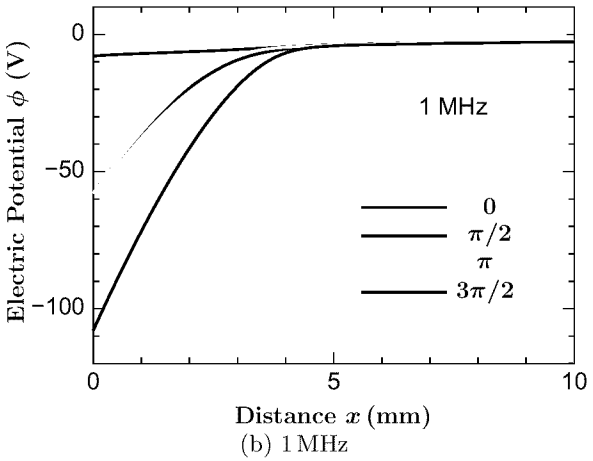

(b) 1 MHz

FIGURE 11. Time-modulation of potential ϕ (10 mTorr).

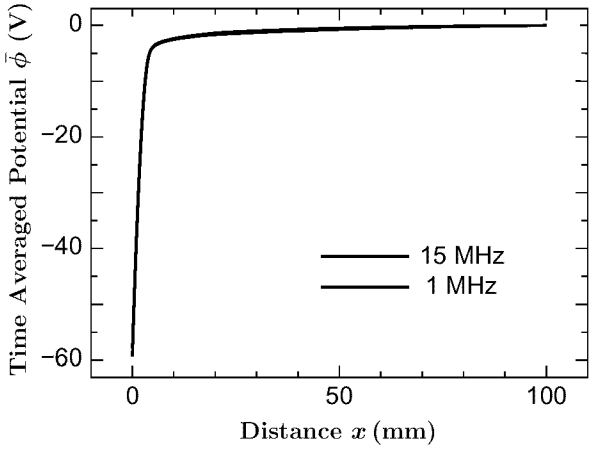

FIGURE 12. Time-averaged potential $\bar{\phi}$ (10 mTorr).

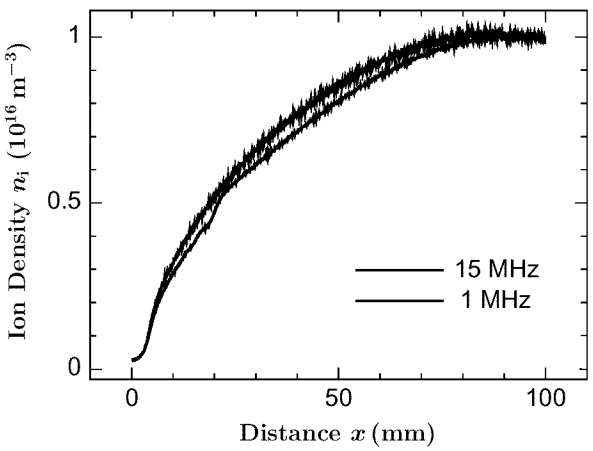

FIGURE 13. Ion density (10 mTorr).

almost constant in the presheath. These results show that the present method is applicable to the numerical analysis of the sheath and presheath.

We then applied our method to the case when the floating wafer is under rf biasing. We fixed the gas pressure at 10 mTorr and examined the effect of the bias frequency on the sheath structure. Our choice is 15 MHz and 1 MHz. The peak-to-peak voltage applied to the wafer is fixed at 100 V. Figures 11(a) and (b) show the time-modulation of the potential $\phi(x, \alpha)$, where $\alpha(= \omega t)$ is the phase of the bias potential. As is shown later, the sheath and presheath boundary is near $x = 5$ mm. Figure 11 shows that the sheath is time-modulated at both low and high frequency. Figure 11(a) shows that in case of high frequency not only the sheath but also the presheath is somewhat time-modulated. Figure 12 shows the time-averaged potential $\bar{\phi}(x)$. The effect of the bias frequency on $\bar{\phi}$ is small. We see that the dc bias is -59.27 V for 15 MHz and -57.86 V for 1 MHz. Figure 13 shows the ion density. The higher ion density at 15 MHz is probably due to a larger rate of ionization. The ion density is hardly time-modulated, as is shown in Figs. 14(a) and (b). Strictly speaking, the ion density is slightly time-modulated at the low frequency, as is seen from Fig. 14(b). The electron density n_e agrees with the ion density n_i in the presheath. However, n_e is time-modulated in the sheath, as is shown in Figs. 15(a) and (b). The electron density is non-zero at the phase of $\pi/2$, at which the wafer works as an instantaneous anode. The time-averaged electron and ion densities are shown in Figs. 16(a) and (b). The charge neutrality breaks at $x = 5$ mm, which is the edge of the sheath. Although the plasma density is higher at 15 MHz, we can see no effect of the bias frequency on the sheath thickness.

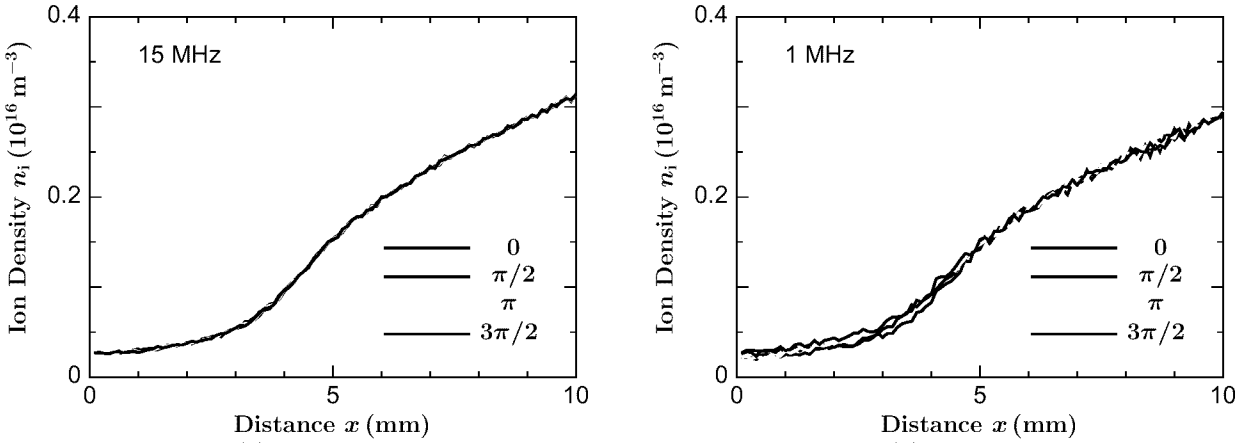

(a) 15 MHz (b) 1 MHz

FIGURE 14. Time-modulation of ion density (10 mTorr).

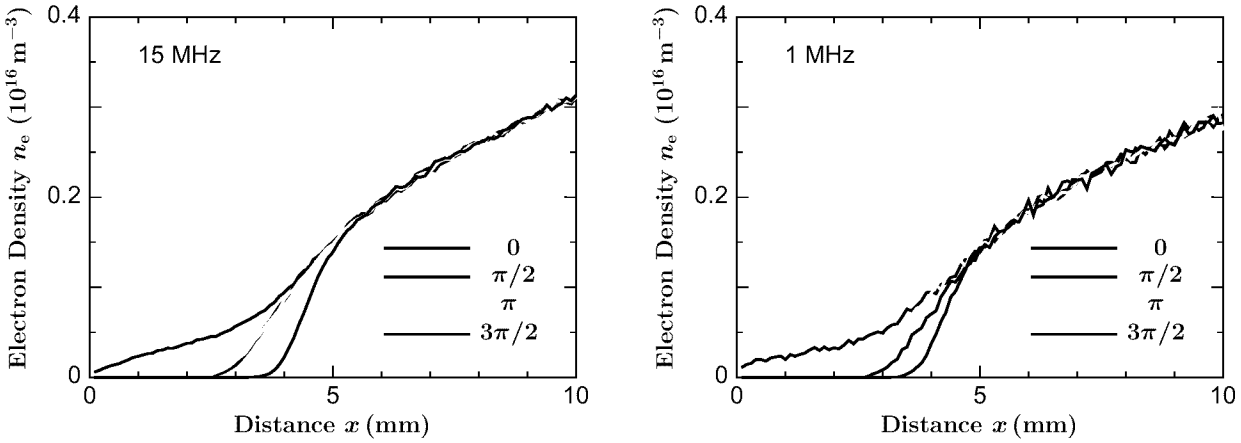

(a) 15 MHz (b) 1 MHz

FIGURE 15. Time-modulation of electron density (10 mTorr).

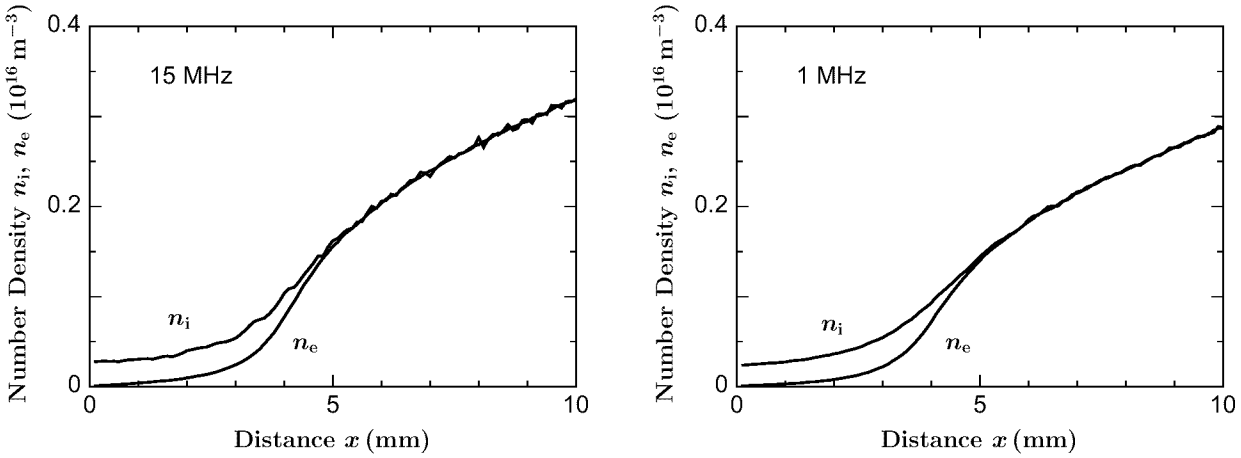

(a) 15 MHz (b) 1 MHz

FIGURE 16. Time-averaged number densities of ion and electron (10 mTorr).

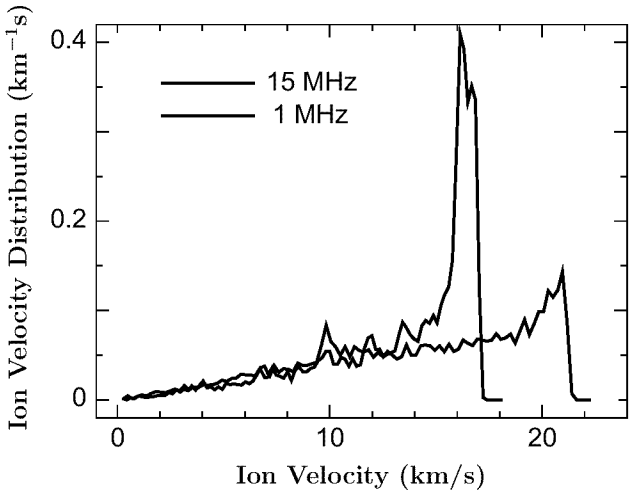

Lastly, the ion velocity distribution function is shown in Fig. 17. The gas pressure is 10 mTorr as before. Owing to Ar^+–Ar collisions, the function does not take the form of twin peaks in Fig. 1. Since the highest velocity is realized in the case of no collision, however, the right side of the peak can be partly interpreted from the analytic expression of eq. (3). In Fig. 1, the location of the right peak is near to $\overline{v}_w + A$. Since A in eq. (2) decreases with increasing ω, the peak in Fig. 17 is shifted with increasing the bias frequency.

V CONCLUSION

The IVD was obtained using the self-consistent particle-in-cell/Monte Carlo simulation. In the case of no rf biasing the dependence of IVD on the background gas pressure was investigated. We found the IVD is more localized toward the upper side of the distribution as pressure decreases. We then calculated the oscillatory sheath potential due to rf biasing. The IVD under wafer biasing is broad due to ion collisions. The shape of IVD in high velocity regime is analogous to the analytic IVD for no collision; the location of the peak is shifted to a lower velocity as the bias frequency increases.

REFERENCES

1. Sugai, H., Nakamura, K., Hikosaka, Y., and Nakamura, M., *J. Vac. Sci. Technol.* A, **13(3)**, 887–893 (1995).
2. Samukawa, S. and Ohtake, H., *J. Vac. Sci. Technol.* A, **14(6)**, 3049–3058 (1996).
3. Sobolewski, M. A., Olthoff, J. K., and Wang, Y., *J. Appl. Phys.* **85**, 3966–3975 (1999).
4. Hoekstra, R. J. and Kushner, M. J., *J. Appl. Phys.* **79**, 2275–2286 (1996).
5. Kinoshita, T., Hane, M., and McVittie, J. P., *J. Vac. Sci. Technol.* B, **14**, 560–565 (1996).
6. Hasegawa, A., Simpuku, F., Hashimoto, K., and Nakamura, M., "The rf bias effect on electron shading damage and the measurement of damage current," in *Proc. 19th Symp. Dry Process*, Inst. Elect. Eng. Jpn., Tokyo, 1997, pp. 15–20.
7. Nasser, M. Ohtsu, Y., Tochitani, G., and Fujita, H., *Jpn. J. Appl. Phys.* **36**, 4722 (1997).
8. Parzen, E., *Modern Probability Theory and its Applications*, New York: Wiley, 1992.
9. Ahn, T. H., *Diagnostics and Silicon Etching in an Inductively-Coupled Pulsed Plasma in Chlorine*, Dissertation, Department of Electrical Engineering, Nagoya Univ., 1997.
10. Nanbu, K. and Wakayama, G., (unpublished).
11. Kosaki, K. and Hayashi, M., *Denkigakkai Zenkokutaikai Yokoshu*, Tokyo: Inst. Electr. Eng. Jpn., (1992) [in Japanese].
12. Peterson, L. R. and Allen, J. E., *J. Chem. Phys.* **56**, 6068–6076 (1972).
13. Nanbu, K. and Wakayama, G., *Jpn. J. Appl. Phys.* **38**, 6097–6099 (1999).
14. Nanbu, K., *Jpn. J. Appl. Phys.* **33**, 4752–4753 (1994).
15. Lieberman, M. A. and Lichtenberg, A. J., *Principles of Plasma Discharges and Materials Processing*, New York: Wiley, 1994.